Fast and accurate metrology of multi-layered ceramic materials by an automated boundary detection algorithm developed for optical coherence tomography data

Peter Ekberg,[1] Rong Su,[1,*] Ernest W. Chang,[2] Seok Hyun Yun,[2] and Lars Mattsson[1]

[1]*Department of Production Engineering, KTH Royal Institute of Technology, 68 Brinellvägen, Stockholm 10044, Sweden*
[2]*Wellman Center for Photomedicine, Massachusetts General Hospital, 50 Blossom St. Boston, Massachusetts 02114, USA*
Corresponding author: rongs@kth.se

Optical coherence tomography (OCT) is useful for materials defect analysis and inspection with the additional possibility of quantitative dimensional metrology. Here, we present an automated image-processing algorithm for OCT analysis of roll-to-roll multilayers in 3D manufacturing of advanced ceramics. It has the advantage of avoiding filtering and preset modeling, and will, thus, introduce a simplification. The algorithm is validated for its capability of measuring the thickness of ceramic layers, extracting the boundaries of embedded features with irregular shapes, and detecting the geometric deformations. The accuracy of the algorithm is very high, and the reliability is better than 1 μm when evaluating with the OCT images using the same gauge block step height reference. The method may be suitable for industrial applications to the rapid inspection of manufactured samples with high accuracy and robustness.   © 2014 Optical Society of America

OCIS codes: (100.0100) Image processing; (100.3008) Image recognition, algorithms and filters; (110.4500) Optical coherence tomography; (120.3940) Metrology; (230.4170) Multilayers.
http://dx.doi.org/10.1364/JOSAA.31.000217

1. INTRODUCTION

With the development of "roll-to-roll multi-layered-material 3D shaping technology," large-scale and cost-effective production of micro devices using advanced ceramic materials is enabled. In parallel, higher demands are put on in-process 3D micrometrology, with requirements of high-precision, rapid, and automated inspection techniques. This has to cover thickness measurements of component layers, determination of shape and dimensions of embedded 3D structures, assessment of free and embedded surface quality, and detection of de-bonding, cracks, warping, and deformations [1].

High dimensional accuracy is needed because, in ceramic components for terahertz frequency applications, variation in alumina thickness can affect the dielectric loss at these sub-mm wavelengths. For ceramic coolers used in automotive lighting systems, the dimensional quality is very important to get the best heat dissipation performance when attached to a high-power LED system. In microfluidic devices, the flow parameters of media are influenced by a change of channel dimensions and surface quality. Moreover, defects such as large residual pores in the ceramic layers significantly influence the thermal conductivities and mechanical strengths of the layers.

Optical coherence tomography (OCT) [2] is a promising technique that provides non-contact and non-destructive 3D inspection with micrometer resolution at high data acquisition rates. Although its applications, to a large extent, are related to the field of biomedical science, it also merges into other areas, such as dimensional metrology, materials research, non-destructive testing, and art diagnostics [3]. The characteristics of OCT make it a promising tool to meet the high demands of quality control and inspection in rolled manufacturing processes, even for highly scattering ceramic materials [4,5].

Two effects come along with the utilization of OCT; namely, large data sets and speckles [6]. In-process OCT inspection on a production line generates a large amount of data, which makes visual observation by an expert very time-consuming or even impossible. Noise and speckle degrade the image quality and, therefore, cause significant uncertainty in the observed position of features; moreover, when a visual observation is made, the habit of the operator can even increase this uncertainty. Thus, an accurate and robust image processing and automated boundary detection algorithm is highly needed.

Published methods of OCT image analysis with segmentation mainly focus on segmenting the intra-retinal layers, tissue structures, and nerve head, but none has been found for industrial applications. Eichel *et al.* [7] proposed a semi-automatic model-based segmentation method. First, the algorithm identifies the layers of the cornea using an enhanced intelligent "scissor," and a correspondence model is established between the upper and lower layers of the cornea. Then, all five boundaries are extracted using a global optimization method, exploiting

the prior information. Garvin *et al.* [8] presented an approach that allowed for the optimal and simultaneous segmentation of multiple 3D surfaces by transforming the segmentation problem into the layered-graph-theoretic problem of finding a minimum-cost closed set in a vertex-weighted geometric graph. A model-based approach was introduced by Kajić *et al.* [9]. During the learning stage, parameters of a statistical model are extracted so that it best fits the training data obtained from manual segmentations by human operators. That includes the possible variation of layer boundaries as well as texture information within the layers. Ghorbel *et al.* [10] used a method based on a global segmentation algorithm, such as active contours and Markov random fields, and a Kalman filter was designed to model the approximate parallelism between the photoreceptor segments and to detect them. Mishra *et al.* [11] have proposed a method based on a classical contour algorithm, which was first proposed by Kass *et al.* [12]. This algorithm has been modified for better handling of OCT retinal tomograms. It is unclear how sensitive the last fine tuning filter is, in practice, for different kinds of images with different feature shapes and resolutions.

It is obvious that most of the authors use filtering and thresholding, but the problem with OCT images is that filtering of speckle is not a trivial task. For this reason, these kinds of filters do not really create an optimum result. Also, all kinds of filtering of images destroy information. Even if an advanced dynamic thresholding algorithm is developed, it will be very problematic to separate real information from false detections caused by the speckle, especially in areas in the image where the signal-to-noise ratio (SNR) is approaching one. The commonly used preset boundary models, which may cause false detection when features are irregular, require computational processes that are usually too complex.

In this paper, we present a novel and simple image processing and segmentation method, of which the performance is largely improved and thoroughly evaluated compared with its previous version in [5]. The final extraction of information is done based on the original OCT image. Therefore, there is no loss of information due to filtering. In the next section, the experimental details of the OCT systems and the ceramic samples are introduced. The details of the algorithm are then described in Section 3 and the algorithm performance is finally evaluated in Section 4.

2. EXPERIMENTAL

A. Fourier-Domain OCT Imaging
OCT is an interferometric technique based on a measurement arm, typically in the axial depth direction, and a reference arm. Instead of mechanically moving a reference mirror or the object being investigated in the axial direction for acquiring the interferogram, the Fourier-domain (FD) OCT detects the spatial frequency spectrum without any mechanical scan. Two types of FD–OCT exist [2]. One is the spectral-domain (SD) OCT that utilizes a spectrometer detector array to obtain the spectral interferogram, and the other is the swept-source (SS) OCT that employs a wavelength-swept laser source with a center wavelength λ_0 and bandwidth $\Delta\lambda$. The latter uses a single photo detector to record the spectrally resolved interferogram sequentially while tuning the wavelength of the light source. The spatial information in the axial direction (A-scan) is then obtained by an inverse Fourier-transform of the spectrally resolved interferogram [2]. By using a galvo

mirror, the beam can be directed to different x-positions, creating a cross-sectional B-scan; by moving the specimen in the y-direction, or using a second galvo mirror, a full 3D volume C-scan is acquired and stored as a 3D intensity map $I(x, y, z)$. By avoiding the mechanical scans in the axial direction, only lateral scans are performed, using a galvo mirror. This significantly enhances the signal acquisition rate. An FD–OCT with near-100 MHz A-scans has been reported by Fard *et al.* [13].

Apart from the advantages of being non-destructive and operating at high speed, the axial resolution of OCT systems is high ($\Delta z \approx 0.44 \cdot \lambda_0^2 / \Delta\lambda$), due to the requirement of a broadband tunable laser. Lateral optical resolution is determined by the numerical aperture (NA) of the objective lens. Usually, a low NA objective is used to achieve a long confocal length and suppress multiple light scattering; whereas, micrometer-level lateral resolution is achieved using a high NA objective.

B. OCT Specifications
In this work, a Thorlabs [14] SS OCT and a laboratory SS OCT [15], operating at 1.3 μm center wavelength, were used for investigating the ceramic samples. The specifications of the systems are given in Table 1.

C. Ceramic Samples
The investigated samples are made from alumina ceramic layers manufactured by tape casting, lamination, laser-machining, and sintering. The layers were provided by Swerea IVF [16] and the laser-machining processes were done at Wrocław University of Technology [17] and at MEC, Cardiff University. The samples were developed for applications in terahertz components, coolers for automotive lighting systems, and microfluidic devices and sensors.

The SEM image presented as Fig. 1 shows the prepared cross section of a sintered alumina sample. The residual pores that are assumed to be filled with air are distributed randomly in the ceramic matrix, where the porosity and the average pore diameter of alumina sample are obtained as 1%–1.8% and 0.4–0.6 μm, respectively. Compared to the crystalline grain boundaries, the pores are more likely to scatter light strongly and cause multiple scattering and speckles in OCT (due to the high refractive index of alumina: $n \sim 1.75$ at $\lambda \sim 1.3$ μm). Therefore, the received intensity and image contrast in the OCT scan are degraded rapidly with increasing depth.

The samples are positioned under the OCT probe to get cross-sectional B-scan images. For example, the marked cross sections 1 and 2 in Fig. 2 represent the imaged sites for a single ceramic layer with a laser-machined channel on top and a double layer stack with an embedded channel.

Table 1.   Specifications of SS OCT Systems

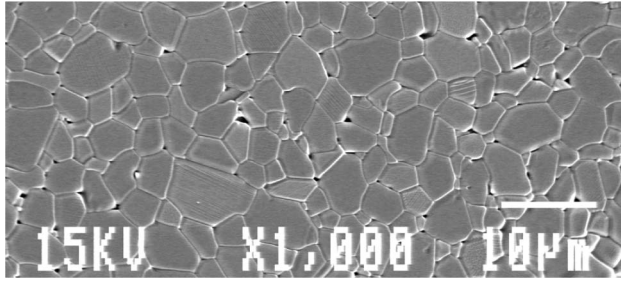|	Thorlabs	Laboratory
Center wavelength	1325 nm	1300 nm
Spectral bandwidth	>100 nm	>110 nm
Axial scan rate	16 kHz	10 kHz
Lateral pixel size	5.86 μm/pixel	7.4 μm/pixel
Axial pixel size	5.86 μm/pixel	4.12 μm/pixel
Lateral resolution	25 μm	<20 μm
Axial resolution	12 μm (in air)	12 μm (in air)

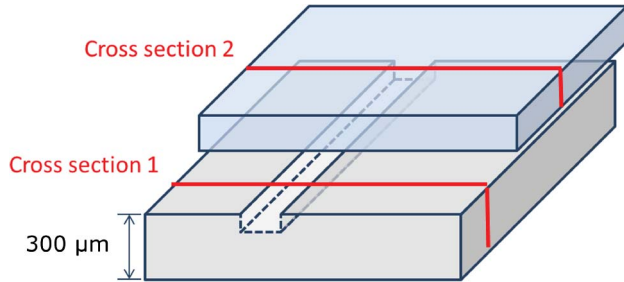Fig. 1. SEM image of the prepared cross section of the sintered alumina sample.

Fig. 2. Geometrical layout of sample stack. Marked cross sections 1 and 2 correspond to OCT imaging planes.

3. NEW BOUNDARY DETECTION ALGORITHM

A. Signal to Be Detected

A typical OCT B-scan image at cross section 2 of Fig. 2 is shown in Fig. 3, and on the right hand side the averaged A-scan intensity profile is shown after integration along each pixel row. The peaks appearing in this A-scan profile represent interfaces in the layered ceramic stack. To make the OCT technique accessible as a metrology tool, we need good algorithms for detecting these edges in the OCT images. A large number of edge detection techniques have been described in the image processing literature [18]. Most of these edge detector algorithms use the first, second, or even the third derivative of the image for extracting the inflection point of the edge transfer function that corresponds to the location of the edge. As an example, the commonly used Canny detector [18] works quite well if the SNR is reasonably high in
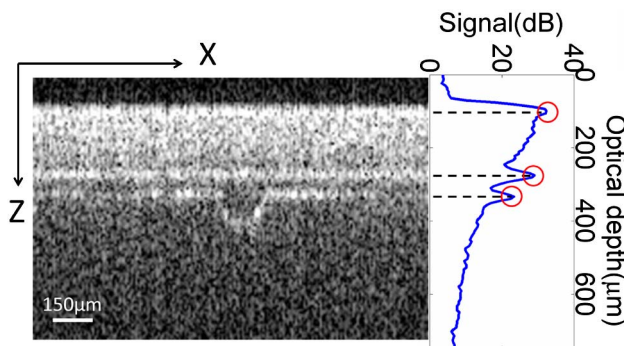

Fig. 3. OCT B-scan of cross section 2 (marked in Fig. 2) and its corresponding average A-scan. The white bar corresponds to 150 μm in the *x*-direction. Optical distance scaled by the refractive index of alumina applies in the *z*-direction in the A-scan profile. Image obtained by the Thorlabs OCT.

the image. In OCT images of biological samples, a layer boundary is usually made up from the assembly of smaller tissue microstructures that sometimes have relatively small changes in refractive index compared to their surroundings. In our case, we are not interested in the scattering particles themselves or grain structures in the alumina ceramic material. On the contrary, the industrial ceramic samples investigated here contain continuous surfaces that exhibit very pronounced air–material interface reflection peaks in OCT images. The geometric shapes and positions of the surface boundaries are the features of interest.

As seen in Fig 3, the three horizontal boundaries can be easily perceived by the human eye. We can use the local image contrast to describe how easy it is to see the brighter interface reflection peaks by a human eye. The local contrast is defined as $C = (I_{max} - I_B)/I_B$, where I_{max} is the signal of the peaks as marked in the above A-scan and I_B is the local background signal level. When the local contrast is too low, human visual perception cannot make an accurate observation of the boundaries. Another metric to assess the quality of OCT images is the SNR. Typically, SNR is defined as the ratio of the mean and standard deviation of the intensity, $\text{SNR} = \langle I \rangle / \sigma$. We know that SNRs of OCT images can be lower than 1 [6], i.e., the OCT images contain a lot of dark spots with an intensity close to zero. This fact makes it practically impossible to use a standard edge detector algorithm to find the interfaces with a high degree of accuracy. In this paper, therefore, we use the defined local image contrast and SNR as metrics to evaluate the performance of our algorithm.

B. Concept

The ultimate algorithm for finding features in the OCT images should use as few tunable parameters as possible. It should be simple, fast, and, of course, be robust against noise. It would also be an advantage if the algorithm does not need any filtering and preset models.

Based on the poor local image contrast present in the OCT images of ceramic samples, we have chosen a different approach for solving the problem of extracting the interface information from these images. The idea of this concept has its root in measuring the so-called "mura" in images of display masks. *Mura* is a Japanese word meaning "not perfect" [19]. Mura is caused by extremely small systematic placement errors of pixels on the mask. In a visual inspection of the mask, these artifacts are seen as weak contrast changes in lines or bands across the mask. In an image of the mask, it is almost impossible to measure these placement errors due to the fact that the error is of the same magnitude, or smaller than the random noise.

In an OCT image, we have a similar case. It is easy for an experienced observer to see features in the image thanks to the human brain's preference for filling in missing information. However, to teach a computer to recognize and measure these interrupted or noisy features is a real challenge. Based on the material characteristics and geometry of the features, we made a major assumption that the real ridges (interface reflection maxima in the OCT image) are longer than false ridges. The latter are caused by speckles and discrete small scatter centers, although we know that the surface profile is continuous everywhere for the alumina layer.

C. Method

The method can be summarized in three steps, as diagrammed in Fig. 4, where the labels A–F correspond to the images in Fig. 5. First, we extract local intensity maxima that will form more or less continuous ridges of pixels. Then, the longer segments are extracted using the assumption of a continuous
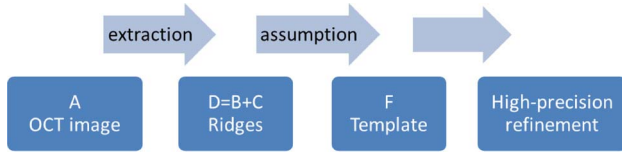

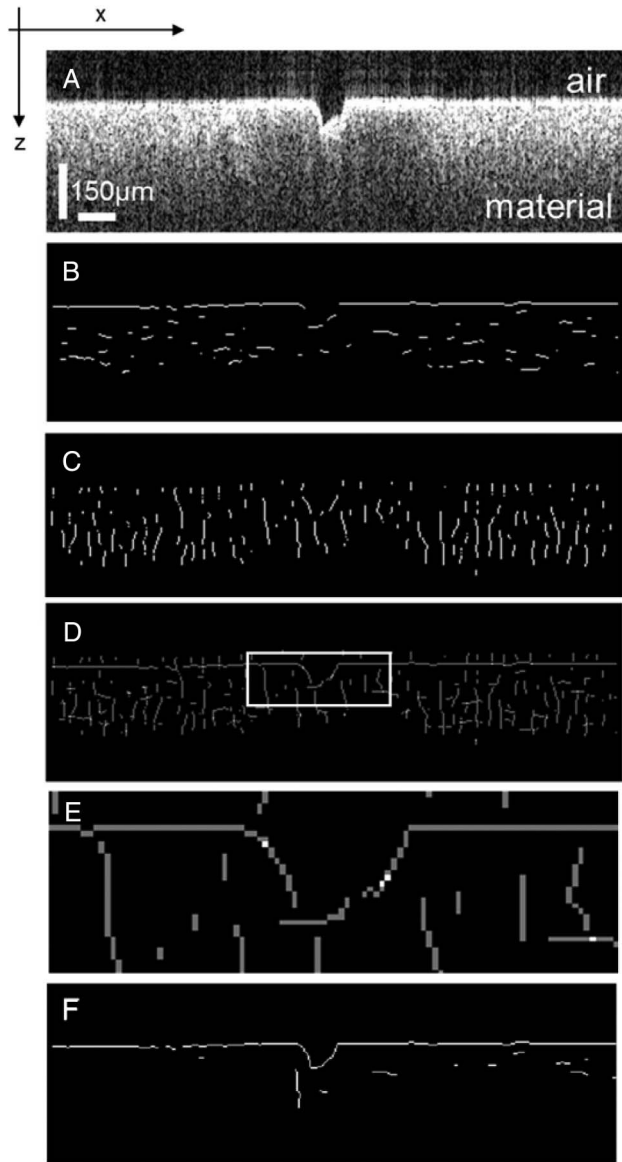Fig. 4. Steps of the new OCT boundary detection algorithm.

Fig. 5. Images describing the different steps in the algorithm. A Input OCT image. B The result after extracting longest ridges in x-direction. C The result after extracting longest ridges in z-direction. D The logical connection map, $D = B + C$. E Enlargement of the connection map marked with a white rectangle in D. F Final logical template of ridges after merging and cleaning process. The vertical bar in A represents a 150 μm optical distance in the material.

surface. A template of the extracted image is built, where the ridges are marked as ones in a logical image with pixel precision. In the final step, a second algorithm is applied on the original OCT image to achieve the sub-pixel-precision refinement.

1. Detection of Intensity Ridges

To demonstrate the method, we use a B-scan of a laser-machined ceramic tape in air. Figure 5 shows six images that represent the steps in the new method. References to this figure will be made in the following two sections of this paper. The input is a cross-sectional OCT image at cross section 1 of Fig. 2, i.e., an alumina layer with a laser-machined groove. This image is shown in Fig. 5A. The task is to extract feature information from the image, which, in this case, is the surrounding air–material interface. This information can be used later for recreating the shape of the channel, curvature, and surface roughness.

The first step is to select a suitable window for extraction of elongated local intensity maxima (ridges) We do that by using a kernel with a size $K_x, K_z = 2 \cdot m + 1, 2 \cdot n + 1$, where m, n are integers. This assures the kernel has a symmetric center point. The kernel is then scanned over the entire image for finding ridges extending in the x-direction. Then, the kernel is rotated 90° and scanned for finding ridges in z-direction. Ridges in any direction will be found by the kernels.

In each pixel location, the following procedure is run (the case is shown for ridges in x-direction only):

The local mean values $\mu x(i,j)$ of the pixels are calculated from the intensities of the pixels covered by the kernel. This is done by convolving the input OCT image $\text{Img}(i,j)$ with the K_x by K_z large kernel (containing only ones) and having its local center $x = 0$, $z = 0$, where $z = -m, -m + 1, \ldots m$ and $x = -n, -n + 1, \ldots n$, and dividing by the number of pixels used in the kernel. This can be expressed mathematically as:

$$\mu x(i,j) = \frac{1}{K_x \cdot K_z} * \sum_{z=-m}^{m} \sum_{x=-n}^{n} \text{Img}(i + z, j + x), \qquad (1)$$

where i is the row index in the OCT image and j is the column index.

In the next step, we calculate the projection vector $Vx_{i,j}$, shown in Fig. 6.
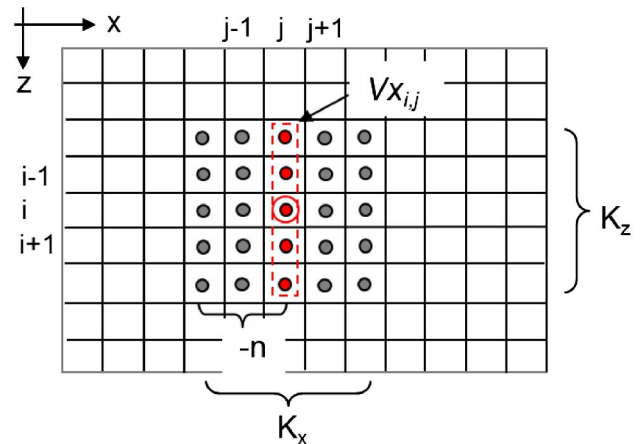

Fig. 6. Principle of the calculation of the projection vector $Vx_{i,j}$.

We generate the following vector $Vx_{i,j}$ of K_z number of elements, where each element with the index k in the interval $[0, K_z - 1]$ around the point i, j is calculated as:

$$Vx_{i,j}(k) = \frac{1}{K_x} * \sum_{x=-n}^{n} \text{Img}(i + k - m, j + x). \qquad (2)$$

As seen, each element in this vector is the mean of K_x number of pixels in x-direction extending from $j - n$ to $j + n$. $Vx_{i,j}$ is, in other words, a projection of K_z number of local mean values. The next step is to estimate the maximum $\mu x_{\max}(i,j)$ and the location of the maximum $Lx(i,j)$ in the vector $Vx_{i,j}$. This can be expressed as:

$$\mu x_{\max}(i,j) = \max(Vx_{i,j}) \qquad (3)$$

$$Lx(i,j) = \arg\ \max(Vx_{i,j}) \qquad (4)$$

After this, we assume that we have a ridge pixel, provided the following logical condition is true:

$$Lx(i,j) = \text{floor}(K_z/2) \qquad (5)$$

where $\text{floor}(K_z/2)$ rounds the elements of $K_z/2$ to the nearest integers less than or equal to $K_z/2$. If $Lx(i,j)$ is equal to the floor $(K_z/2)$, then we have a local maximum in the middle of the vector $Vx_{i,j}$ at location i, j, In such a case, we save the maximum $\mu x_{\max}(i,j)$ in a new image $\text{Img}X(i,j)$ at location i, j. The same procedure is then performed with a rotated kernel for finding ridges in the z-direction. The mathematical expressions for these operations are similar to the above Eqs. (1)–(5). The result is saved in another image $\text{Img}Z(i,j)$.

The size of the kernel (K_x, K_z) should be large to suppress noise as much as possible. However, it is obvious that the spatial resolution, i.e., the ability to detect features with high spatial frequency, will set a limit of the size of the kernel. In the OCT images we have analyzed, we found a proper size is in the range (5,5)–(17,17) pixels for the kernel.

To avoid using ridges in regions of the image where we have very flat "high plateaus," we use a dimensionless measure of the strength of a ridge pixel. These local strength values $Sx(i,j)$ and $Sz(i,j)$ are calculated separately in x- and z-direction s only for the pixels that fulfil condition (5) as:

$$Sx(i,j) = \mu x(i,j)/\mu x_{\max}(i,j), \qquad (6)$$

$$Sz(i,j) = \mu z(i,j)/\mu z_{\max}(i,j). \qquad (7)$$

A regular OCT image is presented in 256 gray levels. The problem now is to set a valid threshold for Sx and Sz. As can be seen from Eqs. (6) and (7), strong local maxima will give large Sx and Sz values; therefore, by choosing a local threshold T_x for Sx and T_z for Sz, we can control the sensitivity of the ridge extracting algorithm separately in each direction, and only ridge pixels with a Sx and Sz above the thresholds will be used in the next step.

When looking at the simple example presented in Fig. 5A, we see that the only interesting information is at the top air–material interface. It is, therefore, not necessary to examine ridges in the entire image. For the purpose of speeding up the algorithm, we thus select a region of interest (ROI). The final logical images used for further processing, ridges*X* and ridges*Z*, are then calculated as:

$$\text{ridges}X(i,j) = 1 \quad \text{if } Sx(i,j) > T_x; 0 \quad \text{if } Sx(i,j) \leq T_x, \qquad (8)$$

$$\text{ridges}Z(i,j) = 1 \quad \text{if } Sz(i,j) > T_z; 0 \quad \text{if } Sz(i,j) \leq T_z. \qquad (9)$$

In Figs. 5B and 5C, the images ridges*X* and ridges*Z* are presented as examples of what pixels are ridges and are left in x-direction and z-direction after the above treatment.

2. Merging Horizontal and Vertical Ridges

When imaging horizontal ceramic layers and measuring layer boundaries extending primarily in an x, y-plane, the ROI will be found in the horizontal x-direction. Therefore, we use the ridges*X* image [Fig. 5B] for a first estimation of ridges containing relevant layer information. As seen in the figure, there are some long ridges but also some gaps, probably caused by surface roughness and speckles, so that pixels in this region did not fulfil condition (5) above. Besides the horizontal air–material interface in the image, we are also aiming for a representation of the laser-machined channel. To fill in the missing pixels of the channel, we use the ridges*Z* image and generate a logical connection map. This map is presented in Fig. 5D. Here, we first generate a cross point image that is simply the sum of the ridges*X* and ridges*Z* images. Since ridges*X* and ridges*Z* are logical images, they just contain "1" in a pixel that is a ridge pixel and "0" for a pixel that is not a ridge pixel. For x- and z-ridges with a common point, the sum will be equal to "2." Thus, a pixel in the cross point image with the value of two is a connection point of two ridges extending in horizontal and vertical directions. The difference in strength, i.e., *if* $Sx(i,j) > Sz(i,j)$, is also marked in the connection map. In this way, we can find the most probable continuation of a ridge at a connection point. As shown in Fig. 5E, the connection points are marked with white pixels and the horizontal and vertical ridges with gray pixels. By using the connection map, we can now merge horizontal and vertical ridges using some simple logic. Horizontal and vertical ridges can only be merged together at a connection point if the following conditions are met:

(1) The connection point is the first or last connection point along a horizontal ridge. Eventual connection points in-between those points are certainly generated by speckle and are, therefore, false ridges.

(2) The ridge to connect to is stronger in the vertical direction at the connection point.

3. Construction of Continuous Features

After the vertical ridges are merged, the eventual short-gaps of, at most, three pixels are bridged (according to the lateral resolution of OCT systems). This bridging is only used temporarily for the construction of the most probable features in the image. After these processes, the final pixel-resolved template is obtained and, for the current case, it is presented in Fig. 5F. Based on this template, we can calculate the actual interface reflection peaks at sub-pixel resolution by applying the subsequent refinement algorithm.

D. Sub-Pixel Refinement Algorithm

In the template, each ridge pixel fulfills condition (5) above. This means that, inside the local kernel with the size K_x, K_z, we know that there is a local maximum at location i, j. We now use a closer neighborhood around this ridge pixel to find where the maximum is located, with sub-pixel precision. The smallest neighborhood you can use is the eight pixels that surround the pixel at location i, j. According to Eqs. (10) and (11), the gradients of these pixels are calculated as eight vectors (black arrows in Fig. 7) pointing toward the locations of the local maxima:

$$\text{grad}X(i,j) = 0.5 \times [\text{Img}(i,j+1) - \text{Img}(i,j-1)], \quad (10)$$

$$\text{grad}Z(i,j) = 0.5 \times [\text{Img}(i+1,j) - \text{Img}(i-1,j)]. \quad (11)$$

The directions are given by the gradient angle:

$$\theta(i,j) = \arctan[\text{grad}Z(i,j)/\text{grad}X(i,j)], \quad (12)$$

and are marked with red dashed arrows in Fig. 7. The neighboring pixels' "opinions" of the locations of the maxima are given by the strength of the gradient in x- and z-direction:

$$S_{XZ}(i,j) = \sqrt{\text{grad}X(i,j)^2 + \text{grad}Z(i,j)^2}, \quad (13)$$

and marked with red dots, which must be inside the white circle to be accepted. The red crosshair that is calculated by averaging the red dots is the sub-pixel location of the maximum at location i, j.

If the location i, j is not a maximum, i.e., less than 6 opinions (the red dots) are accepted for a ridge in x-direction, and no pixels are accepted within the small white square in Fig. 7, then we skip this location without further notice. Otherwise,
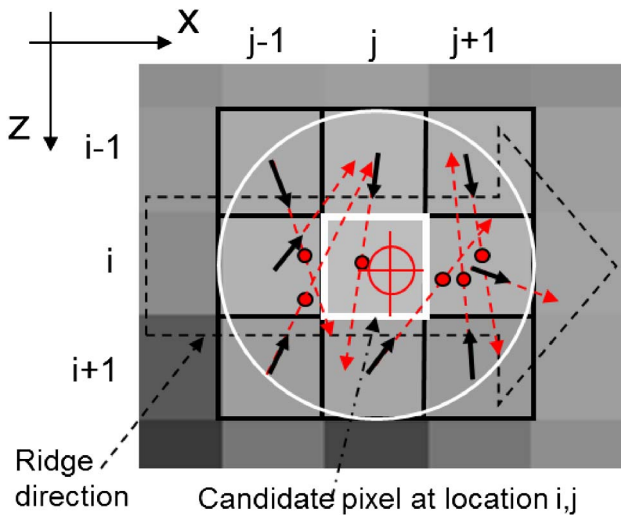

Fig. 7.   Eight pixel neighborhood of a ridge pixel i, j (marked with a white square) belonging to a ridge in x-direction. The black arrows are the gradient vectors, originating at the centers of these eight pixels and pointing toward the locations of the local maxima, which are marked with red dots. The red crosshair that is calculated as the center of gravity of the red dots is the final sub-pixel location of the ridge pixel at location i, j.
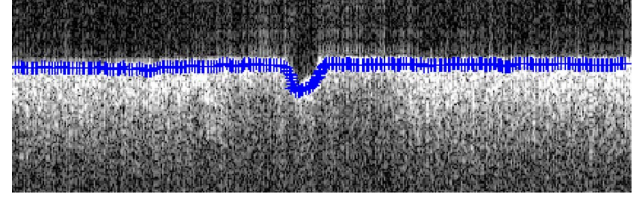

Fig. 8.   Result after the sub-pixel-precision location of each pixel in the template shown in Fig. 5F has been calculated. A few false ridges left in the template will not be accepted in the refinement. Both the horizontal boundary and the highly tilted slope of the channel can be extracted.

the sub-pixel location of the crosshair maximum for the ridge pixel at location i, j will be used, and a chain of pixels describing the ridge with sub-pixel precision is built, as shown in Fig. 8, where the logical template in Fig. 5F is used.

An important feature of this algorithm is its ability to find the true boundary of reflection maxima with sub-pixel precision. Furthermore, it can remove pixels that are not real local maxima in the eight pixel neighborhood, but have been found in a larger area K_x, K_z around location (i, j) by the algorithm described in Section 3.C. The final result is generated using the original OCT image, without loss of information due to filtering effects.

4. RESULTS AND DISCUSSION

A. Evaluation of the Image Processing Algorithm

In the following sections, the performance of the algorithm is evaluated. This is important because, no matter how good the OCT system is, errors in image processing can easily destroy measurement accuracy. However, there are no standard guidelines on how to perform such an evaluation [20], particularly for OCT image processing algorithms. Moreover, we are lacking a standard terminology for describing the goodness of algorithms quantitatively. That relates to the difficulty in finding suitable metrics to provide objective measures of performance [20]. We define the following indicators with reference to Wirth *et al.* [20] for evaluating our algorithm. Note that these indicators are not defined and used in the exactly same way as the metrology terminology [21].

(1) *Accuracy*: how well the algorithm has performed with respect to some reference images or human visual observations.

(2) *Reliability*: the degree to which an algorithm, when repeated using the images of the same reference sample, yields the same result. The reliability is expressed as the standard deviation of the measurement results from these images.

(3) *Sensitivity*: how responsive an algorithm is to small changes in features.

(4) *Robustness*: an algorithm's capacity for tolerating various image qualities.

(5) *Adaptability*: how the algorithm deals with variability in images.

(6) *Efficiency*: the practical viability of an algorithm (time and space).

The overall accuracy is quantitatively indicated by comparing the nominal value with the measured value. However, the discrepancies between these values are caused by: (a) the uncertainty of the OCT system due to optical and mechanical imperfections and environmental influence, and

(b) uncertainty due to the image processing algorithm. These two sources are not easy to evaluate separately; therefore, the latter is also qualitatively evaluated by human visual observations.

It is also important to mention that, when the measured horizontal boundaries are not closely adjacent in depth, the sub-pixel accuracy of the positions of these boundaries can be derived far better than the A-scan OCT axial resolution (see Table 1), as the boundaries are obtained as an average from a large number of pixels along a horizontal line in the B-scan. Thus, the axial resolution is not suitable as an indicator for the accuracy and precision of an OCT system.

In this paper, the evaluation tasks were defined by the demands of an inspection system of the future "roll-to-roll multi-layered 3D shaping technology of ceramic micro devices." The material–air interfaces are extracted from OCT images for measuring thicknesses of component layers, for determining shapes and dimensions of embedded structures, and for detecting deformations and delamination.

B. Accuracy and Reliability

Two pieces of ceramic gauge blocks [22] (height standard) are used to create accurate step heights of 1.005 mm. The maximum permissible error (MPE) is 0.4 μm in height. The layout of the gauge blocks is shown in Fig. 9 and the OCT imaging site is marked with the red line.

In Fig. 10, the OCT image of the 1.005 mm step and the segmented result are shown. The top surfaces are extracted using the described algorithm with sub-pixel precision, and represented by many small crosses. The step height is then calculated as the average distance between fitted lines to the lower and upper surfaces, respectively, given by the interface reflection peaks in the OCT images. The measurement is repeated with the gauge blocks slightly moved to test the reliability of our algorithm. The tilt-compensated result is reported in Table 2 as the average value of the measured step heights,
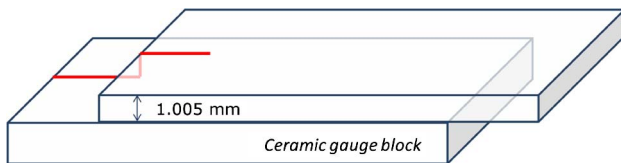

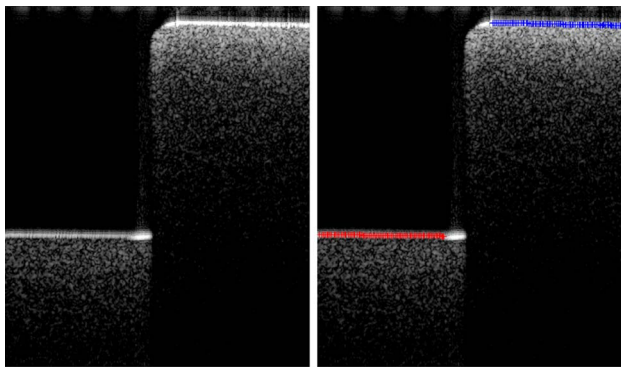Fig. 9.   Schematic layout of the gauge blocks.

Fig. 10.   OCT image of the step height of the ceramic gauge blocks (left). Small crosses represent the extracted boundaries with sub-pixel precision (right). The laboratory OCT system is used.

Table 2.   Step Height of Ceramic Gauge Blocks

Certified gauge block height	1.005 mm ± 0.2 μm
Average measured height	1.0048 mm
Reliability	±0.9 μm

from several different OCT images. The reliability is obtained as the standard deviation of the measured values.

The accuracy is also evaluated with the cross-sectional OCT images of an alumina stack with two embedded channels. The geometric layout of the sample stack is similar to that shown in Fig. 2. The top layer has a thickness of 142 μm, measured using an inductive spherical probe (MPE 0.7 μm) toward a spherical ball, to minimize waviness contributions to the thickness measurement. The average depth of the channels is 64 μm, measured using a well-calibrated Zygo New View 7300 scanning white light interferometer [23]. The root-mean-square (RMS) roughness of the alumina layers is around 60 nm, measured with a Talystep surface profiler (2 μm tip radius and 250 μm profile length). The surface could be much rougher at the channel bottom due to the laser process. A number of adjacent cross-sectional OCT images of the alumina stack are analyzed, and an example is shown in Fig. 11. An excellent agreement between human visual observation and the image processing result is obtained. The quantitative measurement results are listed in Table 3.

The above numerical results show that the overall accuracy is high. The reliability of the algorithm is confirmed only by the ceramic gauge block because the alumina sample is not perfectly flat and, therefore, is not considered a suitable reference sample. The true reliability of the algorithm is actually better than that shown in Table 2 as the errors are partly due to the OCT system and possible environmental changes.

The differences between the nominal and measured values in Table 3 are larger than those in Table 2, which is mainly because of the wavy and rough surfaces of the alumina samples. Moreover, the error of refractive index is unknown when measuring the thickness of the alumina layer. Therefore, the goodness of the algorithm as perceived by the human eyes is also an important evaluation criterion, and we see a perfect overlap of the extracted pixels on the bright lines in Figs. 10 and 11. However, an advantage of the algorithm over the commonly used visual observation technique is that, the fuzzy boundaries in the image, caused by strong reflection at the air–ceramic interfaces, do not affect the algorithm in finding the real interface peaks. Thus, we can conclude that the new boundary detection algorithm is accurate and reliable. In the following section, we will analyze the other four evaluation criteria using different OCT images of our ceramic samples.

C. Sensitivity and Robustness

1. Small Changes in Feature

Deformation and delamination between two stacked ceramic layers are not uncommon in the sintering process. As can be seen in the OCT image of a two-layer alumina stack (Fig. 12), the surfaces of the top layers are curved and the delamination between the two layers creates a thin wedge-shaped air gap. On the left of the image, only one boundary can be seen due to the axial resolution limit of OCT while two boundaries are present at a certain gap distance.
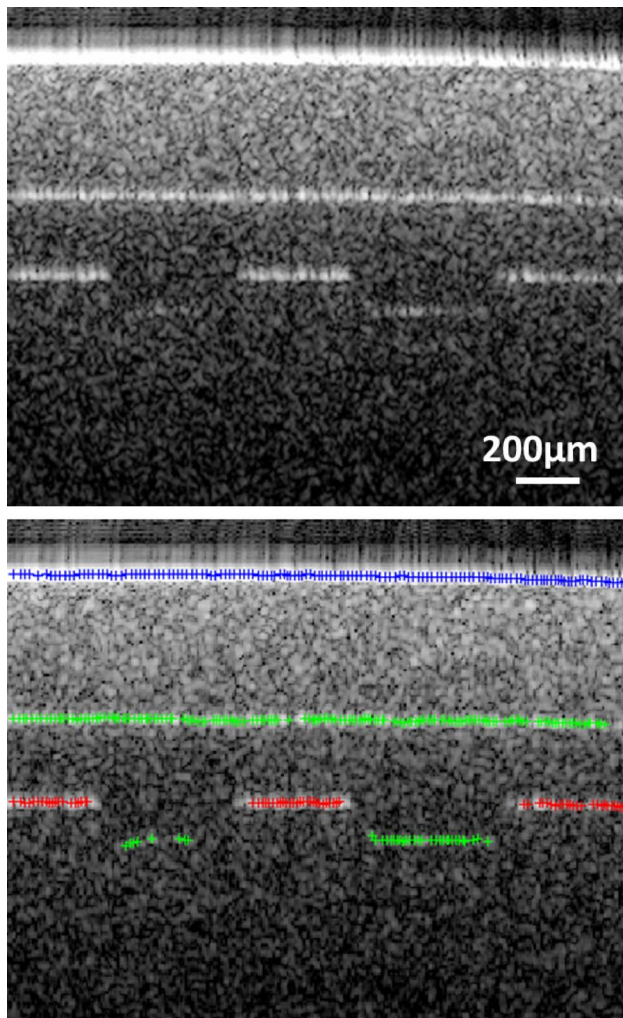
Fig. 11.   Cross-sectional OCT image of an alumina stack with two embedded channels (upper) and the image processing result (lower). The images were captured with the 1.3 μm laboratory OCT system and the layers are segmented simultaneously.

As shown in Figs. 12B and 12C, the algorithm extracts this information quite well and in good comparison with the human visual system. The smallest detectable separation between the two layers is found to be 3.5 pixels (corresponding to 14.4 μm), which is very close to the experimental 12 μm axial resolution limit of this OCT system.

2. Low Quality Noisy Images

Because of light scattering in materials, there is a maximum depth that can be extracted by OCT. By using a wedge-shaped ceramic layer, this depth limit can be found by determining at what depth the rear interface is drowned in noise. This technique is displayed in Fig. 12, which shows the cross section
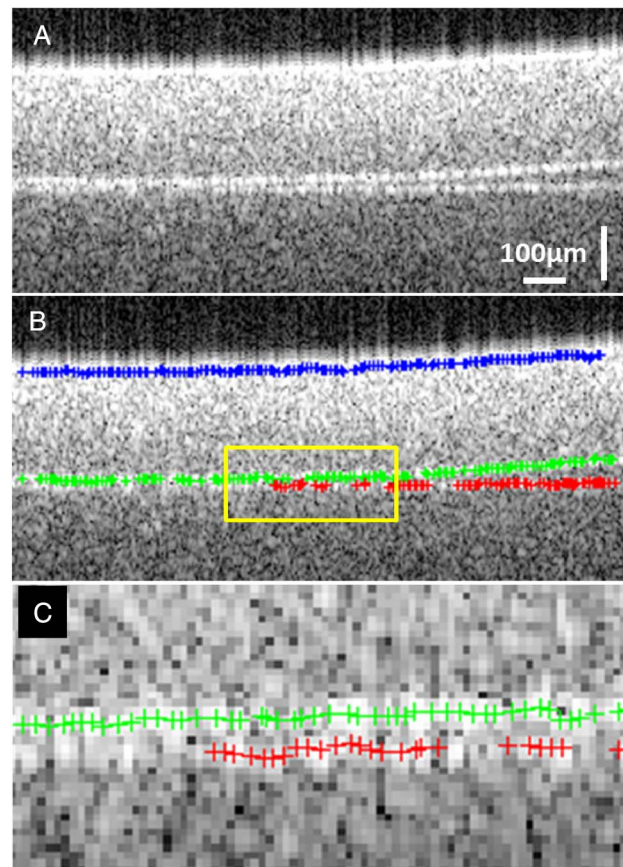
Table 3.   Measurement of Alumina Sample Stack

	Thickness of Top Layer (μm)	Depth of Channel (μm)
Reference value[a]	142	64 ± 2
Measured by OCT	145[b]	66

[a]Measured by the inductive spherical probe and Zygo NV7300.
[b]Theoretical refractive index of alumina at 1.3 μm is 1.75.

Fig. 12.   Cross-sectional OCT images of a two-layer alumina stack with deformation and delamination, as obtained with the 1.3 μm laboratory OCT. A Original OCT image, B the extracted pixels describing each boundary, and C an enlargement of the boundary in the area marked in B. The layers are segmented simultaneously. The vertical bar represents optical distance.

OCT image of a single high-scattering alumina ceramic layer. The image is captured by the laboratory 1.3 μm OCT system and, due to the strong scattering of the material, the rear surface of the alumina layer can hardly be seen. The local image contrast is extremely low (<6%) for the rear surface and the SNR is approaching 1, due to speckles. Also, the significant loss of intensity due to light extinction makes the line segmentation more difficult. However, our algorithm extracts the two boundaries and the extracted pixels overlap on the boundaries precisely, as can be seen in Fig. 13. The rear boundary is not detected as continuous, due to the noise. This extremely difficult test shows that the sensitivity and robustness of the algorithm is very high and the extraction result is comparable to that of human visual observation. The layer thickness is calculated as the optical distance divided by the refractive index (1.746) of alumina at $\lambda \sim 1.3$ μm. Thus, the probing depth of this laboratory 1.3 μm OCT system is 188 μm for this high-scattering alumina.

D. Adaptability

A two-layer alumina ceramic stack with a laser-machined channel in between is used for evaluating OCT images of embedded structures (Fig. 14). The schematic layout has been shown in Fig. 2. The feature in the upward-facing surface of the bottom layer can be considered an embedded micro channel along the direction perpendicular to the page. Without providing the
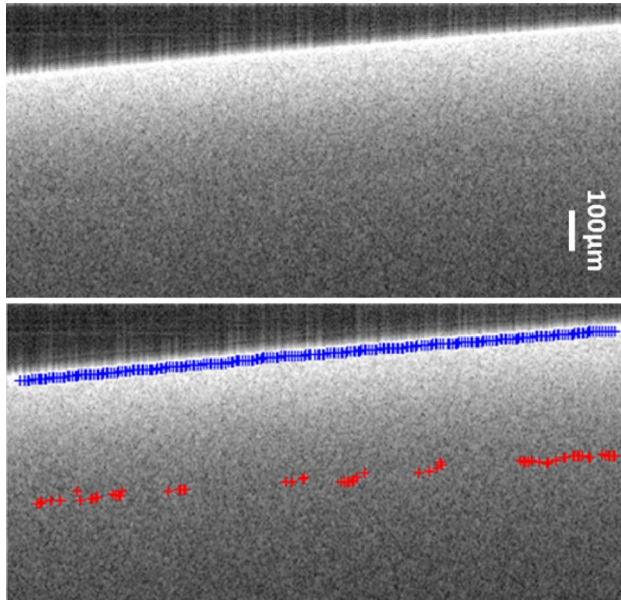
Fig. 13. Cross-sectional OCT image of a single alumina ceramic layer (upper) and the image processing result (lower). The images were captured with the 1.3 µm laboratory OCT system. The vertical bar represents the optical distance.

algorithm with any pre-set model and *a priori* information, the boundaries of the layers and the embedded feature are extracted. The pixels representing the algorithm determined
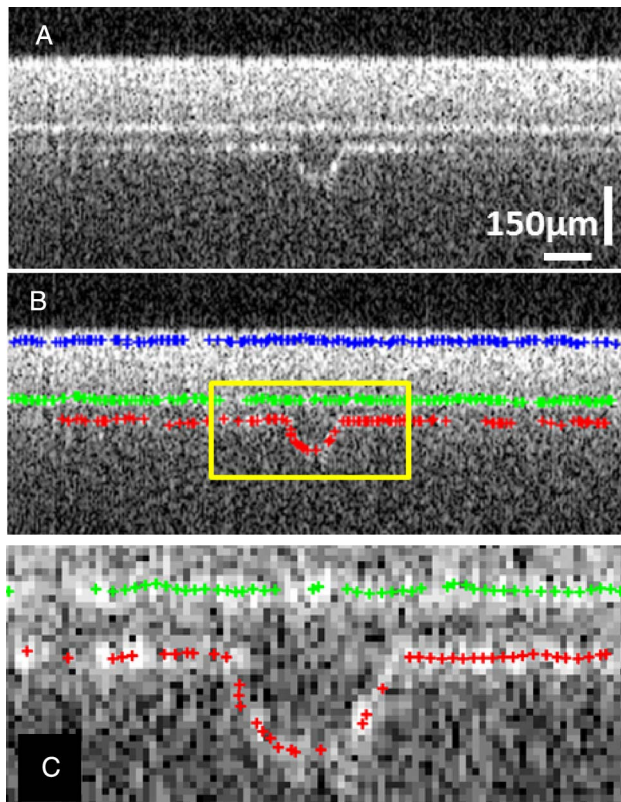

Fig. 14. A Original OCT image and B the extracted boundaries and the embedded channel. C Enlarged graph of the marked area in B. The image was obtained with the Thorlabs OCT and the layers are segmented simultaneously. The vertical bar represents optical distance and the horizontal bar represents geometrical distance.

boundaries that are shown in Fig. 14B. From Fig. 14C, it can be clearly seen that the sub-pixel-extracted crosses follow the channel boundary with very high accuracy, so that the shape and dimensions of the embedded feature can be easily recognized and calculated. This example shows the capability of the algorithm for dealing with arbitrary geometric shapes of the boundaries in OCT images.

E. Efficiency
The algorithm is written in MATLAB and the efficiency is very high, using a normal PC with Intel Core2 Quad CPU Q9400 @2.66 GHz and a 4 GB RAM. Processing time for the OCT image (as shown in Fig. 11), with 280×220 pixels and four boundaries, can be less than 1 s. By optimizing the MATLAB code, an even higher speed can be achieved.

5. CONCLUSION
This paper has presented a new boundary detection algorithm, developed for OCT data suffering from low signal-to-noise levels. It is particularly suited for accurate metrology applications in OCT-captured images. The performance of the image processing and line segmentation, based on our algorithm, was evaluated using six different, and previously recognized, criteria. Based on a large number of OCT images, of which a few are shown in this paper, we find that the algorithm is robust against boundaries with different levels of local image contrast, varying from a few percent to 100%. Images with very low signal-to-noise ratios can also be handled, and results show that the sensitivity of the algorithm is comparable to that of human visual perception.

For the future roll-to-roll multi-layered 3D shaping technology of ceramic materials, the OCT technique has been shown to be a promising technique, as its advantages of high speed, high resolution, and non-destructiveness can be utilized. In an on-line 3D monitoring system of roll-to-roll manufacturing image processing, it is essential to handle large data volumes at high speed and with high accuracy. Our dedicated image processing algorithm is a simple and practical method to extract material boundary information from very noisy OCT images. This information can be further used for measuring thicknesses of component layers, determining shapes and geometric dimensions of embedded structures, and detecting deformations and delamination.

In the future, the authors plan to extend the algorithm for processing volumetric C-scan OCT data, and for extracting the boundaries appearing as intensity gradients in OCT images due to small changes of the refractive index at material interfaces.

REFERENCES
1. S. Bredeau and L. Federzoni, "Multilayer: a large scale production of micro devices via new rolled multi material layered 3D shaping technology," in *Proceedings of the 4 M/ICOMM 2009*

Conference, V. Saile, K. Ehmann, and S. Dimov, eds. (Karlsruhe, 2009), pp. 419–422.

2. A. F. Fercher, W. Drexler, C. K. Hitzenberger, and T. Lasser, "Optical coherence tomography: principles and applications," Rep. Prog. Phys. **66**, 239–303 (2003).

3. D. Stifter, "Beyond biomedicine: a review of alternative applications and developments for optical coherence tomography," Appl. Phys. B **88**, 337–357 (2007).

4. M. D. Duncan, M. Bashkansky, and J. Reintjes, "Subsurface defect detection in materials using optical coherence tomography," Opt. Express **2**, 540–545 (1998).

5. R. Su, M. Kirillin, P. Ekberg, A. Roos, E. Sergeeva, and L. Mattsson, "Optical coherence tomography for quality assessment of embedded microchannels in alumina ceramic," Opt. Express **20**, 4603–4618 (2012).

6. J. M. Schmitt, S. H. Xiang, and K. M. Yung, "Speckle in optical coherence tomography," J. Biomed. Opt. **4**, 95–105 (1999).

7. J. A. Eichel, A. K. Mishra, D. A. Clausi, P. W. Fieguth, and K. K. Bizheva, "A novel algorithm for extraction of the layers of the cornea," in *2009 Canadian Conference on Computer and Robot Vision*, F. Ferrie and M. Fiala, eds. (IEEE, 2009), pp. 313–320.

8. M. K. Garvin, M. D. Abramoff, X. Wu, S. R. Russell, T. L. Burns, and M. Sonka, "Automated 3-D intraretinal layer segmentation of macular spectral-domain optical coherence tomography images," IEEE Trans. Med. Imaging **28**, 1436–1447 (2009).

9. V. Kajić, B. Považay, B. Hermann, B. Hofer, D. Marshall, P. L. Rosin, and W. Drexler, "Robust segmentation of intraretinal layers in the normal human fovea using a novel statistical model based on texture and shape analysis," Opt. Express **18**, 14730–14744 (2010).

10. I. Ghorbel, F. Rossant, I. Bloch, S. Tick, and M. Paques, "Automated segmentation of macular layers in OCT images and quantitative evaluation of performances," Pattern Recogn. **44**, 1590–1603 (2011).

11. A. Mishra, A. Wong, K. Bizheva, and D. A. Clausi, "Intra-retinal layer segmentation in optical coherence tomography images," Opt. Express **17**, 23719–23728 (2009).

12. M. Kass, A. Witkin, and D. Terzopoulos, "Snakes: active contour models," Int. J. Comput. Vis. **1**, 321–331 (1988).

13. A. Fard, C. Wang, O. Malik, G. Fu, A. Quach, K. Goda, and B. Jalali, "Near-100 MHz optical coherence tomography at 800 nm," presented at the First International Symposium on Optical Coherence Tomography for Non-Destructive Testing, Linz, Austria, February 13–14, 2013.

14. Thorlabs, "Swept-source OCT systems," Thorlabs Sweden AB, Mölndalsvägen 3, 400 20 Gothenburg, Sweden. http://www .thorlabs.de/newgrouppage9.cfm?objectgroup_id=2098.

15. U. Sharma, E. W. Chang, and S. H. Yun, "Long-wavelength optical coherence tomography at 1.7 μm for enhanced imaging depth," Opt. Express **16**, 19712–19723 (2008).

16. Swerea IVF, "Ceramic materials," Swerea IVF, Mölndal (head office), P. O. Box 104, SE-431 22 Mölndal, Sweden. http:// swerea.se/en/Start2/Working-Areas/Ceramics/.

17. R. Su, M. Kirillin, D. Jurków, K. Malecha, L. Golonka, and L. Mattsson, "Optical coherence tomography: a potential tool for roughness assessment of free and embedded surfaces of laser-machined alumina ceramic," in *Proceedings of the 8th International Conference on Multi-Material Micro Manufacture*, H. Kück, H. Reinecke, and S. Dimov, eds. (Research, 2011), pp. 140–144.

18. R. C. Gonzalez and R. E. Woods, *Digital Image Processing*, 3rd ed. (Prentice-Hall, 2008).

19. P. Ekberg, "Ultra precision metrology—the key for mask lithography and manufacturing of high definition displays" (Licentiate Thesis, 2011), pp. 17–25.

20. M. Wirth, M. Fraschini, M. Masek, and M. Bruynooghe, "Performance evaluation in image processing," EURASIP J. Adv. Sig. Pr. **2006**, 1–4 (2006).

21. L. Mattsson, V. Schulze, and J. Schneider, "Quality assurance and metrology," in *Ceramics Processing in Microtechnology* (Whittles, 2009), Chap. 22, pp 305–325.

22. T. Doiron and J. Beers, *The Gauge Block Handbook* (National Institute of Standards and Technology, 2009).

23. Zygo NewView7300 3D optical surface profiler, http://www.zygo .com/?/met/profilers/newview7000/.